ACS OMEGA

http://pubs.acs.org/journal/acsodf

Article

Aluminum Doping and Nanostructuring Enabled Designing of Magnetically Recoverable Hexaferrite Catalysts

Pendaranahalli Nadikeraiah Anantharamaiah, Hadonahalli Munegowda Shashanka, Sujoy Saha, Keerthi Haritha, and C.V. Ramana*

Cite This: *ACS Omega* 2022, 7, 6549–6559

Read Online

ACCESS | Metrics & More | Article Recommendations

ABSTRACT: We demonstrate an approach based on substituting a magnetic cation with a carefully chosen isovalent non-magnetic cation to derive catalytic activity from otherwise catalytically inactive magnetic materials. Using the model system considered, the results illustratively present that the catalytically inactive but highly magnetic strontium hexaferrite ($SrFe_{12}O_{19}$; SFO) system can be transformed into a catalytically active system by simply replacing some of the magnetic cation Fe^{3+} by a non-magnetic cation Al^{3+} in the octahedral coordination environment in the SFO nanocrystals. The intrinsic SFO and Al-doped $SrFe_{12}O_{19}$ ($SrFe_{11.5}Al_{0.5}O_{19}$; Al−SFO) nanomaterials were synthesized using a simple, eco-friendly tartrate-gel technique, followed by thermal annealing at 850 °C for 2 h. The SFO and Al−SFO were thoroughly characterized for their structure, phase, morphology, chemical bonding, and magnetic characteristics using X-ray diffraction, Fourier-transform infrared spectroscopy, and vibrating sample magnetometry techniques. Catalytic performance evaluated toward 4-nitrophenol, which is the toxic contaminant at pharmaceutical industries, reduction reaction using $NaBH_4$ (mild reducing agent), the Al-doped SFO samples exhibit a reasonably good performance compared to intrinsic SFO. The results indicate that the catalytic activity of Al−SFO is due to Al-ions occupying the octahedral sites of the hexaferrite lattice; as these sites are on the surface of the catalyst, they facilitate electron transfer. Furthermore, surface/interface characteristics of nanocrystalline Al−SFO coupled with magnetic properties facilitate the catalyst recovery by simple, inexpensive methods while readily allowing the reusability. Moreover, the activity remains the same even after five successive cycles of experiments. Deriving the catalytic activity from otherwise inactive compounds as demonstrated in the optimized, engineered nanoarchitecture of Al-doped-Sr-hexaferrite may be useful in adopting the approach in exploring further options and designing inexpensive and recyclable catalytic materials for future energy and environmental technologies.

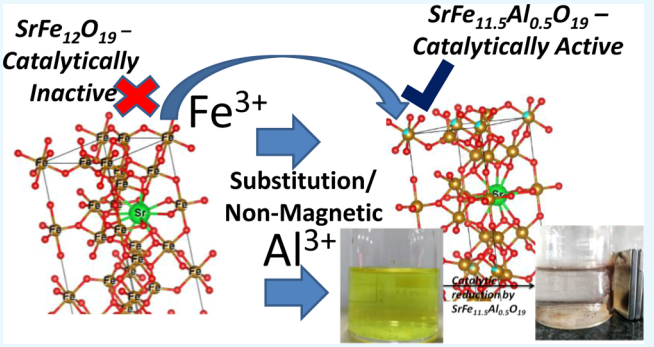

1. INTRODUCTION

Strontium hexaferrite ($SrFe_{12}O_{19}$), which is one among the metal-oxide-based hard magnetic materials, has been widely used in numerous scientific and technological applications.[1−10] $SrFe_{12}O_{19}$ (referred to as SFO hereafter), which belongs to the crystal group of magnetoplumbite, exhibits attractive electromagnetic properties such as a high coercivity (~7000 Oe), a moderate saturation magnetization (~60 emu/g), a high Curie temperature (T_C), and a high remanence (35 emu/g).[1,3,7,11,12] Due to its superior magnetic parameters, high permeability, and low conductivity loss, SFO has been widely used in numerous technological applications, which include permanent magnet designs, microwave absorbers, magnetic recording media and sensors, high-frequency electromagnetic (EM) devices, EM shielding devices, and so forth.[1,3−7,10]

Current interest in SFO and SFO-based hybrids or composite materials at the nanoscale dimensions has been driven by a challenging goal of further enhancing their performance in addition to expanding their potential applicability into other fields, most importantly in energy, health, bio-, and environment-related technologies. In fact, recently, numerous attempts were made to further enhance/improve the magnetic properties of the SFO by metal ion doping, adopting suitable synthesis methods, and optimizing the processing conditions.[2−15] Also, composites of SFO with soft magnetic phases and improved magnetic properties achieved through the exchange-spin mechanism have been

Received: October 5, 2021
Accepted: December 17, 2021
Published: February 14, 2022

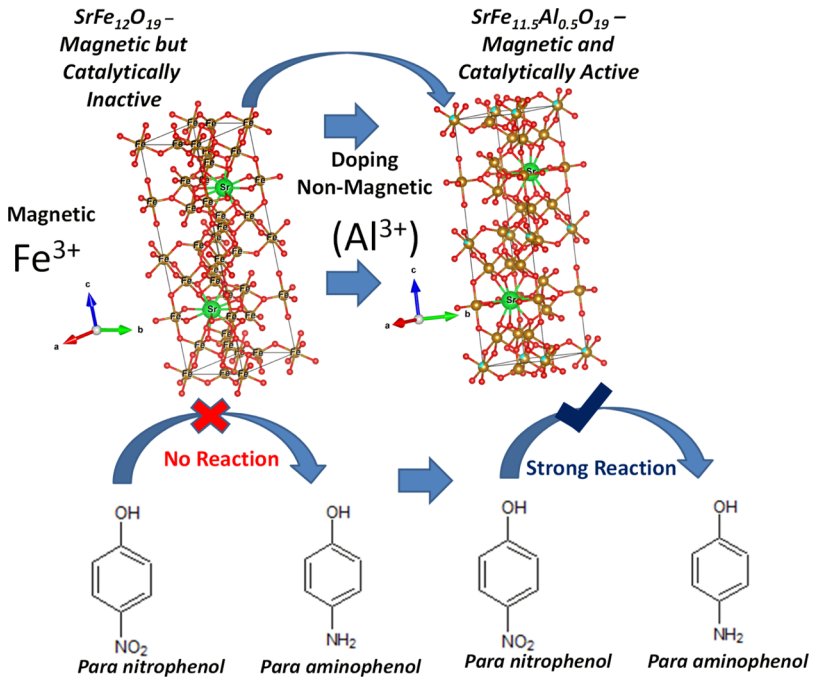

Figure 1. Schematic diagram of the key technical approach employed in this work to derive catalytic activity in SFO by means of Al-doping and surface/interface engineering.

reported in the literature.[3,10,16,17] For instance, using a conducting polymer and a SFO content for tunability, polypyrrole/SFO composites were designed and tested for efficient EM-shielding purposes.[10] It was demonstrated that the electrical and magnetic properties of such composites can be controlled simply by tuning the SFO content. Based on the results obtained using polypyrrole/SFO composites, the authors concluded that the incorporation of magnetic constituents and conducting polymeric materials into multifunctional composites opens new possibilities for the achievement of good shielding effectiveness for various electromagnetic sources.[10] Most recently, magnetic hybrid films containing diblock copolymers (DBCs) and magnetic NPs of SFO were also considered for sensor applications.[2] Spray deposition was applied to prepare perpendicular anisotropic magnetic hybrid films by controlling the orientation of SFO nanoplatelets inside ultra-high-molecular-weight DBC polystyrene-*block*-poly(methyl methacrylate) (PS-*b*-PMMA) films.[2] Using the superconducting quantum interference device data, authors demonstrated that the ferromagnetic hybrid polymer films with high coercivity can be achieved via spray deposition. The spray-deposited hybrid films were reported to be highly promising for potential applications in magnetic data storage and sensing.[2] Similarly, nanostructuring of SFO is shown to enhance the property and performance effectively.[3−7] SFO nanomaterials with highly aligned nanocrystallites combined with crystal growth during spark plasma sintering (SPS) exhibit enormous enhancement of the magnetic properties compared to the as-synthesized powders, leading to high-performance bulk magnets with high-energy products (26 kJ m^{-3}).[4,5] Based on the extensive work, Christensen and team proposed a complete bottomup nanostructuring protocol for preparation of magnetically aligned, high-performance hexaferrite permanent magnets with a record-high $(BH)_{max}$ for dry-processed ferrites.[3,4] Supercritical hydrothermal flow synthesis of anisotropic magnetic-single-domain SFO nanocrystallites of various sizes, and their subsequent compaction into bulk magnets by SPS, followed by thermal treatments enabled design of magnets, energy ratings of which even exceed those of the highest grade commercial magnets produced according to the European, Japanese, and American standards.[4] These considerations of "nanostructuring and composites" are very appealing to combine the nanoscale features and SFO materials' characteristics to design advanced materials for modern technologies. However, while a wealth of information available in the literature toward various approaches to utilize and/or design materials for electromagnetic and electronic applications, designing catalytic materials based on SFO is seldom explored. Therefore, the impetus for the present work is to combine the advantages of nanostructuring, surface/interface engineering, and doping aspects into SFO to design catalytically active materials from an otherwise inactive catalytic system and demonstrate their potential applications in modern pharmaceutical industries. The approach employed in this work to derive catalytic activity from SFO by means of Al-doping and surface/interface engineering is schematically presented in Figure 1. The motivation to design SFO-based catalytic materials for chemical industries is derived from the following considerations.

Magnetically recoverable and recyclable materials, more specifically the magnetic oxide-based nanocomposite materials, have been receiving significant attention for the design and development of novel catalysts due to their applications in numerous chemical industries, including production of bidiesel.[18−21] In fact, in recent years, considerable efforts were directed toward magnetically recyclable solid catalyst design for energy application to meet the demand of green and clean production.[18−20] For instance, Xie et al. have developed magnetically recyclable solid catalysts for the production of biodiesel.[18] The magnetically susceptible Fe_3O_4/MCM-41 composites with a core−shell structure exhibited a strong magnetic response and displayed extraordinary catalytic

https://doi.org/10.1021/acsomega.1c05548
ACS Omega 2022, 7, 6549−6559

activities in the transesterification of soybean oil for the production of biodiesel, with the oil conversion reaching 99.2% by using a methanol-to-oil molar ratio of 25:1 and a catalyst loading of 3 wt % at reflux of methanol after 8 h of the reaction.[18] Moreover, the separation of the solid catalyst from the reaction mixture can be readily achieved by simple magnetic decantation without obvious mass loss, and the solid catalyst can be reused for the heterogeneous transesterification.[18] Similarly, efficient solid hybrid base catalysts based on Fe_3O_4@HKUST-1 composites were reported for clean production.[19] The hybrid catalysts consist of core−shell-structured Fe_3O_4@HKUST-1 composites with a magnetic core and a porous metal−organic framework shell fabricated using a versatile layer-by-layer assembly method, then basic ionic liquids were encapsulated within the core−shell magnetically responsive material.[19] These catalysts exhibited superparamagnetic behavior allowing them for easy separation from the reaction mixture by using an external magnetic field.[19] The solid base catalyst appeared to be an efficient and environmentally benign catalyst for the transesterification of soybean oil with methanol for the production of biodiesel, giving 92.3% oil conversion.[19] Such a catalyst can be readily recovered by simple magnetic decantation and reused several times without significant degradation in its catalytic activity. Additionally, magnetic nanostructured materials containing Fe and Ca synthesized using a simple coprecipitation method were demonstrated to be highly efficient catalysts.[21] Based on these considerations, it is imperative to investigate SFO, which is a widely adopted permanent magnetic material, for catalyst design.

$SrFe_{12}O_{19}$ is a n-type semiconducting material and it has been used as a magnetic component to make composites with various metal oxide-based photocatalysts such as BiOBr and $Bi_4O_5Br_2$.[9,22,23] Therefore, the composites act as catalysts as well as they are magnetic in nature that helps to recover the catalysts from the reaction mixture with a simple, inexpensive method of using a magnet. Thus, catalysts based on such a widely utilized permanent magnetic material may open up the new possibilities for integration into chemical and pharmaceutical industries, where the demand is continuously evolving for catalysts to eliminate or convert toxic and harmful chemical emissions into useful products. Especially, catalysts with possible easy recovery and reusability along with recyclability are highly beneficial in chemical and health sectors,[24,25] and more specifically in pharmaceutical industries. In this context, the present work was performed on designing catalysts based on SFO for utilization in pharmaceutical industries for efficient conversion of toxic pollutants into useful products. To illustratively demonstrate the applicability of doped SFO as a catalyst for pharmaceutical industries, efforts were directed toward the efficient conversion of *para*-nitrophenol chemicals. *Para*-nitrophenol is one of the toxic pollutants being released by pharmaceutical industries. Additionally, nitrophenols are some of the recalcitrant substances, which are considered as high-priority toxic pollutants.[24−30] These are most refractory substances present in industrial wastewaters because of their high stability and solubility in water. The detection, determination, and catalytic conversion of the nitrophenols are, therefore, extremely important. Catalytic conversion of a toxic chemical into a useful and value-added product is the simple and key approach,[24−27] which can be readily integrated to achieve an efficient wastewater treatment technology in both chemical and pharmaceutical industries. Therefore, conversion of nitrophenol into other chemicals such as *para*-aminophenol is highly beneficial as these chemicals can be used as starting materials for industrial dyes, photography development agents, rubber chemicals, and so forth.[24,31−35] While there are recent attempts to design and develop catalysts for the purpose based on environmental friendly, cost-effective, and high-performance materials, catalysts based on noble metals, such as Au, Pd, Pt, Ag, and so forth, have been studied for a long time to convert *para*-nitrophenol to *para*-aminophenol.[25−30,33,36−39] Realizing that the noble metals are expensive, which exhibit sintering and related problems at the nanoscale dimensions, many researchers directed their recent efforts to design and develop various other catalysts, which are based on inexpensive, green, and highly stable metal oxides and/or composites, for the *para*-nitrophenol reduction reaction.[24,28,35,40−44] However, the catalytic studies on the hard magnetic materials such as barium- and strontium-hexaferrites and their derivatives are yet to be explored. On the other hand, based on our previous work on magnetic and electronic materials,[45,46] we recognize that tailoring the materials' structure and controlled phase in nanostructured materials can provide opportunities to design inexpensive nanomaterials for the desired applications. Furthermore, most recently, we demonstrated that the surface/interface magnetic properties can be tailored[46] and have made successful attempts to derive catalytic properties in Cu-substituted strontium hexaferrites synthesized using a tartrate-gel method.[47,48] Therefore, in the present study, Al is chosen for the substitution in place of Fe in $SrFe_{12}O_{19}$ and evaluated its activity toward the nitrophenol reduction reaction. Al^{3+} is a non-magnetic trivalent cation that can be used for substituting isovalent Fe^{3+} in SFO. It has been inferred from our previous studies reported in ref 47 that the catalytic activity more or less remains the same irrespective of dopant concentrations. Hence, we have considered a specific composition of Al-substituted strontium hexaferrite ($SrFe_{11.5}Al_{0.5}O_{19}$). However, we considered a reasonable amount of Al for doping, so that no doping-induced perturbation in the overall magnetic properties of SFO occurs. Also, other non-magnetic trivalent cations such as Ga^{3+} and In^{3+}, although they are isovalent in nature compared to Fe^{3+}, are not suitable as dopants due to their tetrahedral site preference, and these sites are not exposed to the surface of the particles. Interestingly, as presented and discussed in this paper, Al-substituted SFO samples combine the advantages of magnetic and catalytic properties to render economically viable and environmental friendly catalytic nanomaterials.

2. MATERIALS AND METHODS

2.1. Synthesis. Nanocrystalline materials of SFO and $SrFe_{11.5}Al_{0.5}O_{19}$ (Al−SFO) were synthesized using high-purity $Sr(NO_3)_2$, $Fe(NO_3)_3{\cdot}9H_2O$, and $Al(NO_3)_3$ salts as starting materials. We adopted a previously established experimental procedure,[47,48] which is based on the tartrate-gel method, to synthesize the SFO and Al−SFO materials. Briefly, calculated amounts of metal nitrates, which correspond to the $SrFe_{12}O_{19}$ and $SrFe_{11.5}Al_{0.5}O_{19}$ compositions, were weighted into a beaker and dissolved completely with a minimum volume of distilled water. The crystals of tartaric acid (1.5 M/metal ion) were weighed into a 200 mL crystallizing dish and made into a solution with distilled water of the same volume taken for the preparation of metal nitrate solution. Subsequently, metal nitrates and tartaric acid solutions were mixed homogeneously using a magnetic stirrer at 50 °C. In the next step, 2 mL of the

https://doi.org/10.1021/acsomega.1c05548
ACS Omega 2022, 7, 6549−6559

ethylene glycol (acts as a polymerizing agent) was transferred to the above reaction mixture and the temperature of the solution was increased to 80 °C under the same stirring conditions. A brown colored thick viscous gel was found after all the solvent molecules evaporated from the reaction mixture. The viscous gel was dried at 80 °C and crushed into a form of fine powers using a mortar and pestle, followed by calcination at 850 °C for 2 h.

2.2. Characterization. *2.2.1. X-ray Diffraction.* A powder X-ray diffractometer (XRD) [SmartLab, Rigaku X-ray diffractometer (Cu Kα radiation)] was used to probe phase formation and structural aspects of the synthesized materials.

2.2.2. Scanning Electron Microscopy. The scanning electron microscopy (SEM) measurements were carried out on both SFO and Al-doped SFO samples to understand their surface morphology. The measurements were made using a scanning electron microscope (TESCAN VEGA 3LMU). In order to compare and understand the effect of Al-substitution, the samples were imaged under the identical conditions.

2.2.3. Fourier Transform Infrared Spectroscopy. A Fourier transform infrared (FTIR) spectrometer (Bruker, Alpha-P, Diamond ATR cell) was employed to record the FTIR spectra of the samples.

2.3. Catalytic Properties and Performance. *2.3.1. Catalytic Performance.* To investigate the catalytic activity of the synthesized hexaferrite materials, the conversion reaction of *para*-nitrophenol to *para*-aminophenol is chosen as a model chemical reaction. The detailed procedure employed for the purpose of evaluating catalytic property and performance is as follows. Initially, a large volume of 0.2 mM of 4-nitrophenol (4-NP) solution was prepared. 100 mL of 0.2 mM 4-NP solution was transferred into a 250 mL beaker. Later, $NaBH_4$ crystals (equivalent to a concentration of 0.2 M), a mild reducing agent, were mixed with the 4-NP solution and stirred vigorously to make the solution more uniform. After mixing $NaBH_4$ with the 4-NP solution, it is noticed that the pale yellow color of the 4-NP solution turned into a dark yellow color solution due to the formation of a phenolate anion, which exhibits a resonance effect. The UV−visible spectrum of the solution containing the phenolate anion was recorded, and an absorption band was found at a wavelength of 400 nm. 10 mg of the prepared catalyst was mixed with the *para*-nitrophenolate solution and time-dependent UV−visible spectra of the reaction were recoded to examine the catalytic performance of the prepared catalysts. Furthermore, using standard practices, the reaction kinetics also evaluated.

2.3.2. UV−vis−NIR Spectroscopy. The catalytic activity and the extent of chemical reaction and/or progress have been measured by means of the optical absorption measurements. The optical absorption measurements were performed using a UV−visible spectrophotometer (Shimadzu UV-2600). The time-dependent UV−visible optical spectra of the catalytic reaction of 4-nitrophenol were recorded.

2.3.3. Catalyst Recovery and Magnetism. Catalyst recovery measurements were carried out based on the testing and confirmation of samples that showed catalytic properties. The coexistence of catalytic and magnetic activity is believed to help in faster recovery of the catalyst that too using a simple and inexpensive method. Therefore, room-temperature magnetic characteristics of the calcined SFO and Al−SFO samples were investigated using a vibrating sample magnetometer (VSM) (EG&G PAR 4500), After confirmation of magnetic property, the catalyst recovery was attempted by using a simple magnet.

3. RESULTS AND DISCUSSION

3.1. Crystal Structure and Phase. The XRD data of SFO and Al-doped SFO are shown in Figure 2. Both the samples

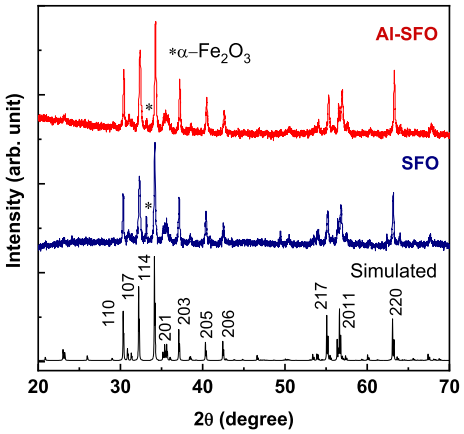

Figure 2. XRD patterns of the SFO and Al-SFO samples. The data compared with the indexed $SrFe_{12}O_{19}$ pattern (generated using the PCW program).

exhibit prominent peaks that correspond to the strontium hexaferrite phase. However, comparison of the XRD patterns of the samples with the simulated powder pattern of $SrFe_{12}O_{19}$ reveals that both samples show a small quantity of the hematite (α-Fe_2O_3) impurity phase along with the prominent peaks corresponding to SFO (see, Figure 2). The formation of an α-Fe_2O_3 impurity phase can be expected when the $SrFe_{12}O_{19}$ sample is heat treated at lower temperatures.[14] As suggested in the literature, the temperature required to form a single phase of $SrFe_{12}O_{19}$ would be ≥1000 °C. Extra line broadening associated with the diffraction peaks of the samples signifies that the materials are nanocrystalline in nature. The average crystallite size estimated using the Scherrer relation is ∼40 nm for SFO. The average crystallite size of the Al−SFO sample is ∼35 nm, which is slightly lower than that of intrinsic SFO. The size reduction, although not very significant, is due to the effect of dopant Al ions, which increases the overall surface energy and, thereby, causes a size reduction. It is well documented in the literature that whenever a foreign element/ion is substituted into the spinel/hexagonal ferrite lattice structure, the local strain will be developed due to size mismatch.[49,50] Here, the ionic size of Al^{3+} is considerably smaller than that of Fe^{3+} and therefore local lattice strain will be generated that is reflected in the peak broadening. Peak broadening indicates a decrease in the particle size and an increase in the surface area. As the surface area of the hexaferrite particles is proportional to the surface energy, there is an increase in the surface energy due to Al-incorporation into the lattice structure of strontium hexaferrite. Also, the surface energy is directly proportional to the number of broken bonds present on the surface of the nanoparticles. When the size of the particles is decreased, one can find a more number of broken bonds on the surface of the particles.

The effect of Al-doping is reflected in the diffraction peaks, where the peak position of Al-doped SFO indicates a positive shift. Such a peak shift to a higher 2θ angle compared to

https://doi.org/10.1021/acsomega.1c05548
ACS Omega 2022, 7, 6549−6559

intrinsic SFO is due to a decrease in the unit cell parameters. The decrease in the lattice parameters is primarily due to the size difference of Al substituted for Fe in SFO. Thus, the lattice reduction is mainly due to the replacement of a bigger cation (Fe^{3+}) of size 0.645 Å for 6-fold coordination by a smaller cation (Al^{3+}) of size 0.55 Å for 6-fold coordination.[51]

To extract further information about the lattice parameter values and percentage of the impurity phase in both intrinsic and Al-doped SFO samples, the Rietveld refinement analysis was performed. The results of the refined patterns are presented in Figure 3. A good fit is obtained for both samples

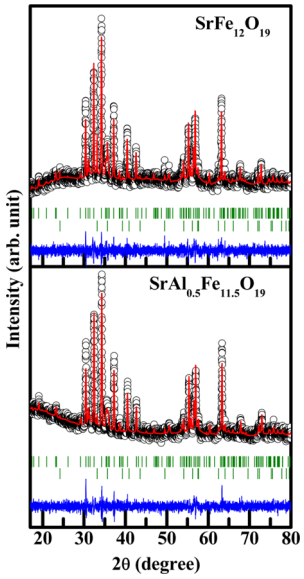

Figure 3. Rietveld fit XRD patterns of the SFO and Al−SFO samples.

as revealed from the fitting parameters such as R_p, R_{wp}, R_{exp}, and χ^2. The values of structural parameters and percentage of the strontium hexaferrite phase and impurity phases are tabulated in Table 1. As revealed from the refinement analysis, the percentage of the impurity phase also decreases from 9.2 to 2.2% after replacing a small fraction of Fe by Al in the hexaferrite lattice structure.

3.1.1. Surface Morphology. The surface morphology of the SFO and Al−SFO samples is shown in Figure 4. As is evident from the SEM images, no significant changes in the morphology of ferrite particles are observed even after replacing a larger-sized magnetic cation (Fe^{3+}) by a smaller-sized non-magnetic cation (Al^{3+}) in the lattice structure of SFO. Although the samples were heat-treated (calcined) relatively at a high temperature (850 °C), the hexaferrite particles are nanocrystalline in nature with an average size of ∼40 nm, which is in agreement with the crystallite size computed from the XRD data. The majority of the particles exhibit a plate-like morphology and this is due to the fact that the samples tend to crystallize in the hexagonal structure.

3.2. Chemical Bonding. Chemical bonding analyses using spectroscopic methods provide direct information on the chemical bonding and dopant-induced changes (if any).[52,53] We found that the FTIR measurements were useful to understand the effect of metal-ion-substitution on the magnetic ion site in simple and complex metal oxides.[42,49] Therefore, in the present work, we relied on FTIR measurement to probe the Al-substitution-induced changes in the chemical bonding in SFO nanomaterials. Figure 5 shows the FTIR spectra of

Table 1. Structural and Rietveld Refined Parameters of the SFO and Al−SFO Samples

$SrFe_{12}O_{19}$					
$SrFe_{12}O_{19}$ hexagonal ($P6_3/mmc$)					
lattice parameters: $a = b = 5.87985$ Å, $c = 23.05185$ Å, vol. = 690.191 Å^3, $\alpha = \beta = 90°$, $\gamma = 120°$				B (Å^2)	phase fraction (vol.)
Sr	2/3	1/3	1/4	0.167	90.80
Fe1	0	0	0	0.949	
Fe2	0	0	1/4	0.680	
Fe3	1/3	2/3	0.02847	0.802	
Fe4	1/3	2/3	0.19142	0.166	
Fe5	0.16257	0.32512	0.89031	0.843	
O1	0	0	0.15581	1.0	
O2	1/3	2/3	0.94881	1.0	
O3	0.18309	0.36618	1/4	1.0	
O4	0.16451	0.32903	0.05303	1.0	
O5	0.50519	0.98962	0.15458	1.0	
Fe_2O_3 hexagonal (R-3c)					
lattice parameters $a = b = 5.03379$ Å, $c = 13.74132$ Å, vol. = 301.543 Å^3, $\alpha = \beta = 90°$, $\gamma = 120°$				B (Å^2)	phase fraction
Fe	0	0	0.35114	0.412	9.20
O	0.37442	0	1/4	1.0	
$R_p = 1.65$, $R_{wp} = 2.12$, $R_{exp} = 1.86$, $\chi^2 = 1.31$					
$SrAl_{0.5}Fe_{11.5}O_{19}$					
$SrFe_{12}O_{19}$ hexagonal ($P6_3/mmc$)					
lattice parameters: $a = b = 5.86915$ Å, $c = 23.00891$ Å, vol. = 686.399 Å^3, $\alpha = \beta = 90°$, $\gamma = 120°$				B (Å^2)	phase fraction (vol.)
Sr	2/3	1/3	1/4	0.643	97.76
Fe1/Al1	0	0	0	0.880	
Fe2	0	0	1/4	0.954	
Fe3	1/3	2/3	0.02810	0.549	
Fe4	1/3	2/3	0.19114	0.162	
Fe5	0.16285	0.32567	0.89071	0.737	
O1	0	0	0.15708	1.0	
O2	1/3	2/3	0.94993	1.0	
O3	0.18161	0.36323	1/4	1.0	
O4	0.15336	0.30675	0.05250	1.0	
O5	0.49869	0.99737	0.15476	1.0	
Fe_2O_3 hexagonal (R-3c)					
lattice parameters $a = b = 5.02966$ Å, $c = 13.74385$ Å, vol. = 301.104 Å^3, $\alpha = \beta = 90°$, $\gamma = 120°$				B (Å^2)	phase fraction
Fe	0	0	0.35949	0.270	2.24
O	0.27653	0	1/4	1.0	
$R_p = 1.55$, $R_{wp} = 2.01$, $R_{exp} = 1.76$, $\chi^2 = 1.31$					

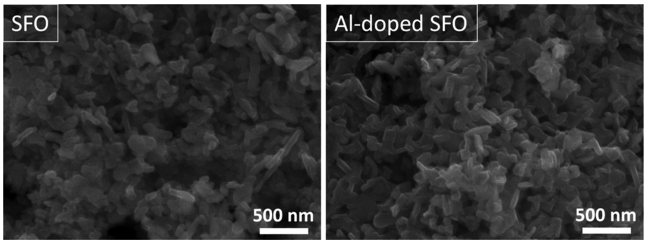

Figure 4. SEM images of the calcined SFO and Al−SFO samples. Images are on the same scale and magnified for better correlation.

SFO and Al−SFO samples. The data shown are spectra recorded at room temperature in the wavenumber range of 300

https://doi.org/10.1021/acsomega.1c05548
ACS Omega 2022, 7, 6549−6559

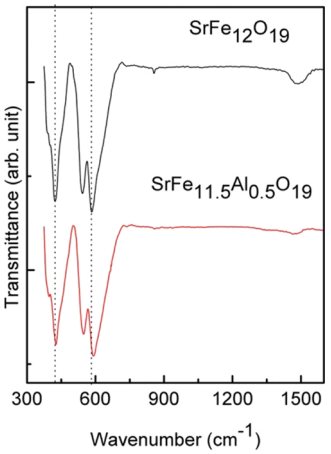

Figure 5. FTIR spectra of the SFO and Al−SFO samples. The effect of Al-substitution is evident in the absorption band shifts.

to 1600 cm^{-1}. The FTIR spectra show the characteristic absorption bands of vibrations of a typical hexaferrite system. In the FTIR spectrum of intrinsic SFO, the bands appearing at the wavenumbers of 583.3 and 423.2 cm^{-1} are attributed to stretching vibrations of tetrahedral metal−oxygen (M_{tetra}−O) and octahedral metal−oxygen (M_{octa}−O) bonds, respectively. Interestingly, these bands are accompanied by shoulders at lower wavenumbers due to the contribution of neighboring cations and anions.[49] As expected, the effect of Al-substitution is the resulting positive shift of tertrahedral and octahedral bands of SFO. It should be noted that these two bands shifted considerably toward higher wavenumbers after incorporating Al ions into the lattice structure of parent SFO. This can be interpreted based on the changes in the bond length and atomic weight. As the size and atomic weight of Al^{3+} are relatively smaller than those of Fe^{3+}, the Al−O bond length is shorter than the Fe−O bond length. As a result, a higher energy is required to stretch the chemical bonds formed in Al−SFO. Hence, a blue shift is observed for the Al-substituted SFO. Thus, corroborated with XRD measurements and structure refinement analyses, the FTIR data reveal the chemical quality of SFO and Al−SFO compounds in addition to confirming the presence of Al- and Al-substitution-induced changes in the chemical bonding in SFO.

3.3. Catalytic Performance. To assess the catalytic properties and evaluate the performance, the SFO and Al−SFO samples were tested as catalysts to drive the 4-nitrophenol reduction reaction under the influence of a weak reducing agent, $NaBH_4$. The *para*-nitrophenol solution is pale yellow in color and changes into a dark yellow color after the addition of $NaBH_4$ due to the formation of a phenolate anion. The absorption band of the *para*-nitrophenolate anion appears at a wavelength of ∼400 nm in the UV−visible spectrum.[24,26] Although $NaBH_4$ is a reducing chemical agent, it cannot convert *para*-nitrophenol to *para*-aminophenol due to a high energy barrier between phenolate and borate anions.[24,26] It is possible to drive the same reaction in the presence of a catalyst, provided if it is active. The time-dependent UV−visible spectra of the SFO and Al−SFO samples, taken at different time intervals, are shown in Figure 6. It is evident that the intensity of the absorption band located at ∼400 nm (*para*-nitrophenolate anion band) remains unaffected even after 25−30 min, indicating that the parent compound is catalytically inactive toward nitrophenol reduction. However, on the other hand, the remarkable effect of Al-doping into SFO toward catalytic activity is clearly visible in the optical data. Unlike the intrinsic SFO, the Al-substituted strontium hexaferrite is catalytically active as manifested in the intensity of the ∼400 nm band, due to the phenolate anion, decreasing with a simultaneous increase in the intensity of the ∼303 nm band, due to *para*-aminophenol, with an increase in the reaction time. At the end of 50 min, the *para*-nitrophenol is completely converted into a *para*-aminophenol. The presence of Al^{3+} ions at the octahedral coordination sites of the hexaferrite is the prime reason for the observed catalytic activity. As the octahedral sites are exposed to the surface of the catalyst, the presence of Al^{3+} ions in octahedral sites facilitates rapid electron, proton, and hydride (electron-rich species) transfer and hence the reduction chemical reaction.

The possible mechanistic pathway for the nitrophenol reduction reaction using the Al−SFO nanocatalyst is illustrated in Figure 7. The hydrogens of the borohydride $[BH_4]^-$ ion form a complex with Al ions, present in the octahedral sites and exposed to the surface, to result in aluminum hydride. Along with hydrogen, the nitrophenolate anion also gets adsorbed over the surface of the catalyst. Now, the hydrogens of the aluminum hydrides could interact electrostatically with oxygen of nitro groups adsorbed on the surface of the Al−SFO catalyst, enabling the elimination of oxygen and reduction of nitro (NO_2) groups. Due to a large electronegativity difference between the residual nitrogen of the NO_2 group and the carbon of the benzene ring, the H atoms of the H_2O molecules, present in the reaction medium, could effortlessly combine

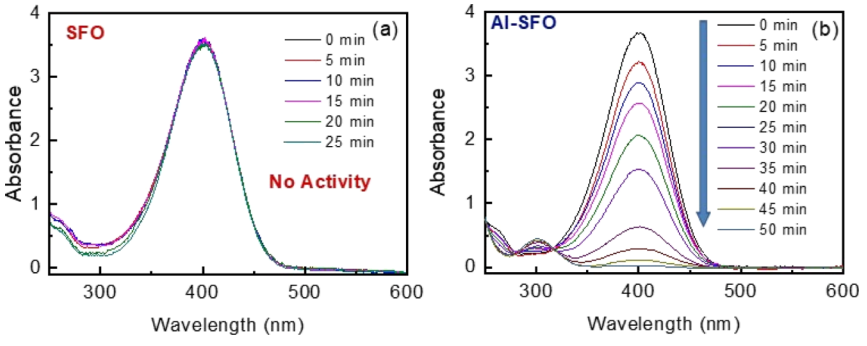

Figure 6. Optical absorption (UV−visible) spectra of *para*-nitrophenol conversion using (a) intrinsic SFO and (b) Al-doped SFO catalysts. The data shown are as a function of time. Intrinsic SFO shows no catalytic activity even for an extended period of time. The Al-substitution-induced catalytic activity in Al-doped SFO is clearly evident.

https://doi.org/10.1021/acsomega.1c05548
ACS Omega 2022, 7, 6549−6559

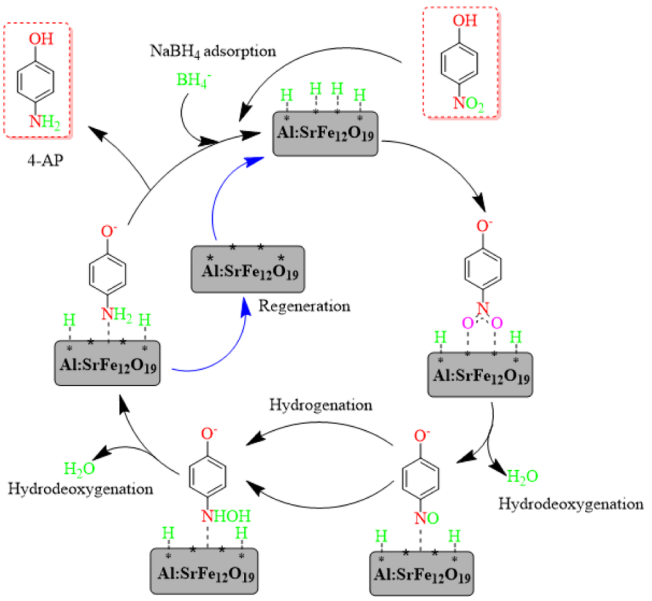

Figure 7. Possible mechanistic pathway for the *para*-nitrophenol reduction reaction using the synthesized Al-doped $SrFe_{12}O_{19}$ nanocatalyst.

with the residual nitrogen (negatively charged species) of the nitrophenol leading to the formation of aminophenol as a final product. Once the nitrophenol is transformed completely into aminophenol, the final product will be detached from the surface of the catalyst and the catalyst will be regenerated. In addition to the proton transfer and deoxygenation processes, electron transport must take place simultaneously from the hydride to *para*-nitrophenol through the Al−SFO catalyst substrate to compensate for the charge balance and achieve the reduction process.[54,55]

The kinetics (rates) of a chemical reaction helps us to understand whether the reaction is progressing slower, moderate, or faster. For most of the reactions, the catalyst will be added into the reaction medium in order to achieve a final product of the reaction in a less period of time. If a chemical reaction is driven by a catalyst, the catalyst will be regarded as a best catalyst when the rate of the reaction is relatively faster. Determination of the rate constant of the reaction is one of the best ways to assess the performance of the catalyst. In the present study, the concentration of $NaBH_4$ is relatively higher than the nitrophenol concentration and therefore the reaction is considered as the pseudo-first-order reaction, which can be written as

$$-k_1(t) = \ln[C_t/C_o] \quad (1)$$

where k_1 is the reaction rate constant, t is the reaction time, C_o is the relative concentration at time zero (initial concentration), and C_t is the concentration at time "t" (which is the time interval during the catalytic reaction).

The SFO sample is found to be catalytically inactive and, hence, its rate constant is negligible. On the other hand, the rate constant for the nitrophenol reduction reaction under the influence of Al−SFO catalysts is found to be 0.05 min^{-1} (see Figure 8). While the first attempt to derive catalytic activity from SFO by Al-doping is successful, we believe that there may be further options that allow us to further tune the surface/interface properties and further reduce the nanocrystal size improving the surface sites to promote the catalytic reaction.

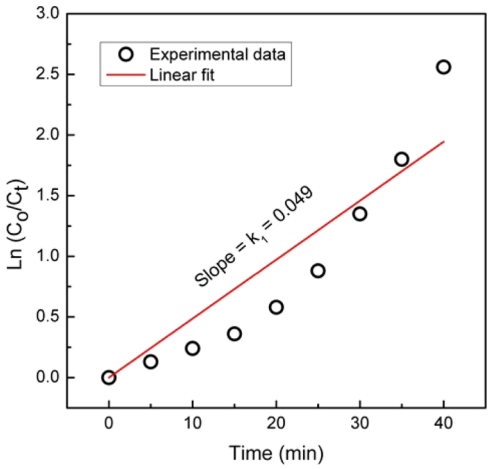

Figure 8. Plot of ln (C_o/C_t) vs time for the catalytic reduction of nitrophenol using the Al−SFO catalyst. The data points are fitted with a linear function to obtain the reaction rate constant.

3.4. Catalyst Recovery and Reusability. Our approach to recovery and reusability is relied on the combined magnetic and catalytic activities, which coexist in the Al-doped sample. Therefore, for the purpose of catalyst recovery, we first consider the magnetic properties of Al-doped SFO compared to SFO. The magnetic field-dependent magnetization of the SFO and Al−SFO samples is presented in Figure 9. These

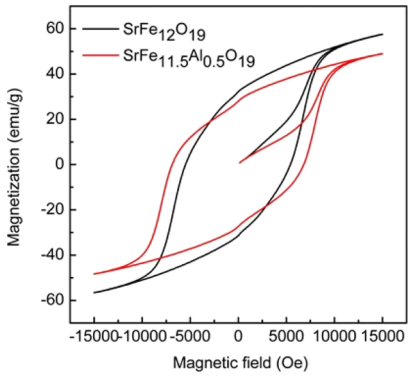

Figure 9. Field-dependent magnetization curves of the SFO and Al−SFO samples.

magnetic data were recorded under ambient conditions. It is evident (Figure 9) that both samples exhibit well-defined hysteresis loops with high magnetic parameters (saturation magnetization, remanence, and coercivity) indicating hard magnetic nature of SFO and Al-SFO samples. The values of M_s, H_c, and M_r of the samples, obtained from the magnetization loops, are tabulated in Table 2. It is interesting note that, after replacing a magnetic cation (Fe^{3+}) by a non-magnetic cation (Al^{3+}) with similar ionic charges from the lattice structure of hexaferrite, the M_s value decreases from 59.4 to 50.5 emu/g. However, the value of H_c was found to be

Table 2. Magnetic Parameters of the Calcined $SrFe_{12}O_{19}$ and $SrFe_{11.5}Al_{0.5}O_{19}$ Samples

sample	MS (emu/g)	HC (Oe)	M_r (emu/g)
$SrFe_{12}O_{19}$	59.4	5482	33
$SrFe_{11.5}Al_{0.5}O_{19}$	50.5	6888	28

https://doi.org/10.1021/acsomega.1c05548
ACS Omega 2022, 7, 6549−6559

increased considerably from 5482 to 6888 Oe. A similar feature of increase in H_c has been reported for the Al-doped strontium hexaferrite in the literature.[7,15] The decrease in M_s and the increase in H_c for the Al-substituted SFO can be understood based on the two primary considerations. The crystallite size of Al-doped SFO smaller than that of the parent counterpart (SFO) is the first. Note that the smaller the crystallite size the lower will be M_s and higher will be H_c.[15] The later consideration or reason for the observed variation in M_s and H_c values is based on the dopant site occupation effect. The dopant ion (Al^{3+}) is a non-magnetic cation and occupies $4f_2$, $4f_1$, 2a, and 12k crystallographic sites of the hexaferrite. As a result, the dopant cation affects the anisotropy constant weakly but strongly affects M_s and hence a strong decrease in M_s and an increase in H_c for the Al-doped SFO compared to intrinsic SFO.

Thus, as revealed from the magnetic property measurements and characterization, similar to intrinsic SFO, Al-substituted SFO is also magnetic in nature. Therefore, magnetic properties of the catalyst should facilitate the easy recovery of the catalyst from the heterogeneous reaction mixture using a simple magnet. To test the validity of this hypothesis, we used a magnet to recover the Al-doped SFO catalyst. As demonstrated in Figure 10, the Al-doped SFO catalyst was easily recovered by simple means. Therefore, clearly and as demonstrated in this work, advantage of developing magnetic based catalysts is one can get rid of tedious filtration and centrifugation methods for the recovery of the catalysts.

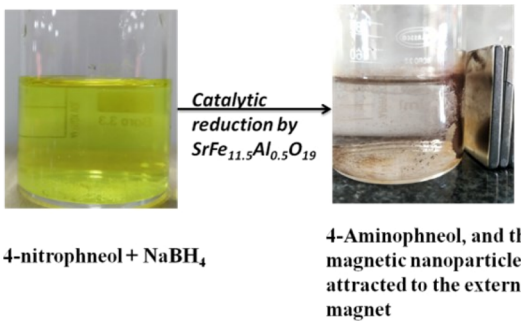

Figure 10. Recovery of the catalyst using a magnet, after the catalytic reaction. The photographs are taken by the authors during experiments in the laboratory.

In order to investigate repeatability and reusability of the Al−SFO catalyst toward nitrophenol reduction, we have performed five consecutive cycles under the identical conditions. After completion of each cycle, the catalyst was recovered from the reaction mixture using a magnet (as demonstrated in Figure 10) and washed several times with distilled water, followed by ethanol and dried thoroughly. The dried catalyst was used for the next cycle. After each cycle, there was a loss of a small amount of the catalyst and volume of the nitrophenol solution was taken according to the weight of the catalyst for the successive cycles. The time-dependent optical absorbance spectra of fifth cycle are presented in Figure 11a and the corresponding residual activity percentage of the catalysts as a function of number of cycles is given in Figure 11b. Even after five successive cycles, the activity was found to remain the same signifying the robustness of the designed Al−SFO catalyst.

Finally, to shed some light toward the merit and future applications, the Al-SFO nanocatalysts prepared in this work exhibit all the features of a catalyst. These Al−SFO nanomaterials characterized by the presence of nanocrystalline particles present a high surface area and appreciable catalytic activity while no catalytic activity exists in intrinsic SFO, with an excellent magnetic behavior that is high enough for simple separation by means of a magnet. Furthermore, as revealed from the repeatability and reusability measurements of the Al−SFO catalyst for nitrophenol reduction, these magnetic Al−SFO nanomaterial-based catalysts can be reused several times without significant loss of their catalytic activity. Thus, all these features, such as catalytic activity toward nitrophenol reduction, good stability, easy recovery, and no loss in catalytic activity after several cycles, which are particularly desirable for industrial applications, make Al−SFO interesting for further studies to employ them in conjunction with other potential candidates so as to design and develop efficient catalysts for energy and environmental applications.

4. SUMMARY AND CONCLUSIONS

In conclusion, we have synthesized Al-doped strontium hexaferrite nanocrystals and demonstrated their catalytic properties and performance while such characteristics were

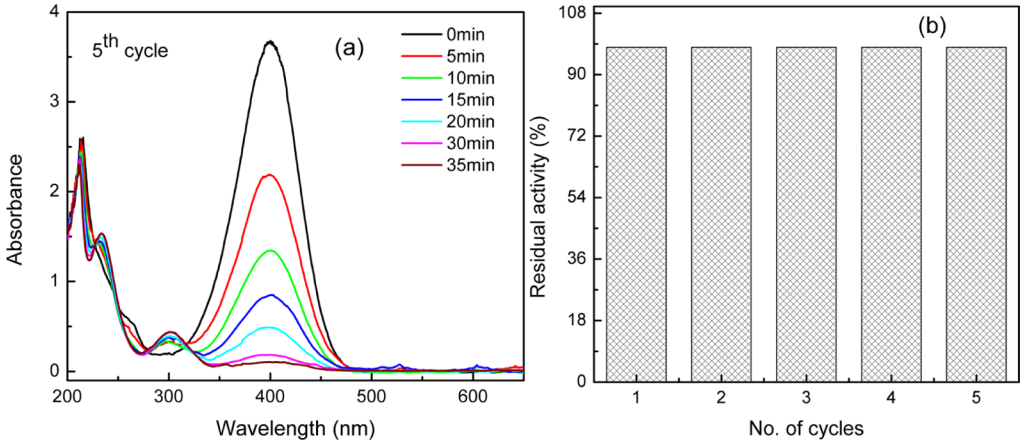

Figure 11. (a) Fifth cycle time-dependent optical absorption (UV−visible) spectra of *para*-nitrophenol conversion using the Al-doped SFO catalyst and (b) percentage of residual catalytic activity as a function of number of cycles.

https://doi.org/10.1021/acsomega.1c05548
ACS Omega 2022, 7, 6549−6559

fully absent in intrinsic strontium hexaferrite. The Al−SFO nanomaterials were synthesized using a simple approach, which can facilitate further tuning of the materials' structure and properties. XRD and FTIR analyses indicated that Al ions are successfully assimilated into the lattice structure of strontium hexaferrite. Due to the non-magnetic nature of Al^{3+} and its octahedral site preference, a considerable decrease in the magnetization and increase in the coercivity have been observed for the Al−SFO samples. The Al−SFO nanomaterials can be employed as a catalyst for the *para*-nitrophenol reduction reaction under mild reaction conditions. The Al−SFO samples exhibit good catalytic activity compared to the parent compound due to the presence of Al^{3+} ions at the octahedral sites, and these sites are exposed to the surface of the strontium hexaferrite catalyst. Furthermore, magnetic properties similar to parent SFO makes recovery of the Al−SFO catalyst readily possible as tested and validated in this work. Furthermore, as revealed from the repeatability and reusability measurements of the Al−SFO catalyst for nitrophenol reduction, these magnetic Al−SFO nanomaterial-based catalysts demonstrate that they can be reused several times without significant loss of their catalytic activity. The physical and chemical properties, such as a large surface area, inexpensiveness of raw materials, relatively low preparation cost and toxicity, excellent stability, good coercivity, low Curie temperature, and recovery and reusability coupled with recyclability, make the nanomaterials with combined magnetic and catalytic properties highly useful for industrial applications. Therefore, our future efforts will be directed to further refine the size and morphology and/or other dopants to explore possible options to further enhance the catalytic efficiency.

AUTHOR INFORMATION

Corresponding Author

C.V. Ramana − *Center for Advanced Materials Research and Department of Mechanical Engineering, University of Texas at El Paso, El Paso, Texas 79968, United States;* orcid.org/0000-0002-5286-3065; Email: rvchintalapalle@utep.edu

Authors

Pendaranahalli Nadikeraiah Anantharamaiah − *Department of Chemistry, Faculty of Mathematical and Physical Sciences, M. S. Ramaiah University of Applied Sciences, Bangalore 560058, India*

Hadonahalli Munegowda Shashanka − *Department of Chemistry, Faculty of Mathematical and Physical Sciences, M. S. Ramaiah University of Applied Sciences, Bangalore 560058, India*

Sujoy Saha − *Department of Materials Engineering, Indian Institute of Science, Bangalore 560012, India*

Keerthi Haritha − *Environmental Science and Engineering, University of Texas at El Paso, El Paso, Texas 79968, United States*

Complete contact information is available at: https://pubs.acs.org/10.1021/acsomega.1c05548

Notes

The authors declare no competing financial interest.

ACKNOWLEDGMENTS

C.V.R. acknowledges, with pleasure, support from the National Science Foundation (NSF) with NSF-PREM grant #DMR-1827745.

REFERENCES

(1) Pullar, R. C. Hexagonal ferrites: A review of the synthesis, properties and applications of hexaferrite ceramics. *Prog. Mater. Sci.* **2012**, *57*, 1191−1334.

(2) Cao, W.; Yin, S.; Plank, M.; Chumakov, A.; Opel, M.; Chen, W.; Kreuzer, L. P.; Heger, J. E.; Gallei, M.; Brett, C. J.; Schwartzkopf, M.; Eliseev, A. A.; Anokhin, E. O.; Trusov, L. A.; Roth, S. V.; Müller-Buschbaum, P. Spray-Deposited Anisotropic Ferromagnetic Hybrid Polymer Films of PS-b-PMMA and Strontium Hexaferrite Magnetic Nanoplatelets. *ACS Appl. Mater. Interfaces* **2021**, *13*, 1592−1602.

(3) Guzmán-Mínguez, J. C.; Ruiz-Gómez, S.; Vicente-Arche, L. M.; Granados-Miralles, C.; Fernández-González, C.; Mompeán, F.; García-Hernández, M.; Erohkin, S.; Berkov, D.; Mishra, D.; de Julián Fernández, C.; Fernández, J. F.; Pérez, L.; Quesada, A. FeCo Nanowire−Strontium Ferrite Powder Composites for Permanent Magnets with High-Energy Products. *ACS Appl. Nano Mater.* **2020**, *3*, 9842−9851.

(4) Saura-Múzquiz, M.; Granados-Miralles, C.; Andersen, H. L.; Stingaciu, M.; Avdeev, M.; Christensen, M. Nanoengineered High-Performance Hexaferrite Magnets by Morphology-Induced Alignment of Tailored Nanoplatelets. *ACS Appl. Nano Mater.* **2018**, *1*, 6938−6949.

(5) Atuchin, V. V.; Vinnik, D. A.; Gavrilova, T. A.; Gudkova, S. A.; Isaenko, L. I.; Jiang, X.; Pokrovsky, L. D.; Prosvirin, I. P.; Mashkovtseva, L. S.; Lin, Z. Flux Crystal Growth and the Electronic Structure of BaFe12O19. *J. Phys. Chem. C* **2016**, *120*, 5114−5123.

(6) Saura-Múzquiz, M.; Granados-Miralles, C.; Stingaciu, M.; Bøjesen, E. D.; Li, Q.; Song, J.; Dong, M.; Eikeland, E.; Christensen, M. Improved Performance ofSrFe12O19 Bulk Magnets through Bottom-up Nanostructuring. *Nanoscale* **2016**, *8*, 2857−2866.

(7) Shirsath, S. E.; Kadam, R. H.; Batoo, K. M.; Wang, D.; Li, S. Co−Al-Substituted Strontium Hexaferrite for Rare Earth Free Permanent Magnet and Microwave Absorber Application. *J. Phys. D: Appl. Phys.* **2021**, *54*, 024001.

(8) Maltoni, P.; Sarkar, T.; Barucca, G.; Varvaro, G.; Locardi, F.; Peddis, D.; Mathieu, R. Tuning the Magnetic Properties of Hard−Soft $SrFe12O19/CoFe_2O_4$ Nanostructures via Composition/Interphase Coupling. *J. Phys. Chem. C* **2021**, *125*, 5927−5936.

(9) Xie, T.; Liu, C.; Xu, L.; Yang, J.; Zhou, W. Novel Heterojunction Bi2O3/SrFe12O19 Magnetic Photocatalyst with Highly Enhanced Photocatalytic Activity. *J. Phys. Chem. C* **2013**, *117*, 24601−24610.

(10) Jiang, J.; Ai, L.; Li, L. Multifunctional Polypyrrole/Strontium Hexaferrite Composite Microspheres: Preparation, Characterization, and Properties. *J. Phys. Chem. B* **2009**, *113*, 1376−1380.

(11) Elansary, M.; Belaiche, M.; Ahmani Ferdi, C.; Iffer, E.; Bsoul, I. New Nanosized Gd−Ho−Sm doped M-type Strontium Hexaferrite for Water Treatment Application: Experimental and Theoretical Investigations. *RSC Adv.* **2020**, *10*, 25239−25259.

(12) Almessiere, M. A.; Slimani, Y.; Baykal, A. Structural and Magnetic Properties of Ce-doped Strontium Hexaferrite. *Ceram. Int.* **2018**, *44*, 9000−9008.

(13) de Julián Fernández, C.; Sangregorio, C.; de la Figuera, J.; Belec, B.; Makovec, D.; Quesada, A. Progress and Prospects of Hard Hexaferrites for Permanent Magnet Applications. *J. Phys. D: Appl. Phys.* **2021**, *54*, 153001.

(14) Shashanka, H. M.; Anantharamaiah, P. N.; Joy, P. A. Magnetic Parameters of $SrFe_{12}O_{19}$Sintered from a Mixture of Nanocrystalline and Micron-Sized Powders. *Ceram. Int.* **2018**, *45*, 13592−13596.

(15) Luo, H.; Rai, B. K.; Mishra, S. R.; Nguyen, V. V.; Liu, J. P. Physical and Magnetic Properties of Highly Aluminium Doped Strontium Ferrite Nanoparticles Prepared By Auto-Combustion Route. *J. Magn. Magn. Mater.* **2012**, *324*, 2602−2608.

https://doi.org/10.1021/acsomega.1c05548
ACS Omega 2022, 7, 6549−6559

(16) Roy, D.; Anil Kumar, P. S. Exchange Spring Behavior in $SrFe_{12}O_{19}$-$CoFe_2O_4$ Nanocomposites. *AIP Adv.* **2015**, *5*, 077137.
(17) Alipour, A.; Torkian, S.; Ghasemi, A.; Tavoosi, M.; Gordani, G. R. Magnetic Properties Improvement Through Exchange-Coupling in Hard/Soft $SrFe_{12}O_{19}$/Co Nanocomposite. *Ceram. Int.* **2021**, *47*, 2463−2470.
(18) Xie, W.; Wan, F. Basic ionic liquid functionalized magnetically responsive Fe_3O_4@HKUST-1 composites used for biodiesel production. *Fuel* **2018**, *220*, 248−256.
(19) Xie, W.; Han, Y.; Wang, H. Magnetic Fe_3O_4/MCM-41 composite-supported sodium silicate as heterogeneous catalysts for biodiesel production. *Renewable Energy* **2017**, *125*, 675−681.
(20) Krishnan, S. G.; Pua, F.-L.; Zhang, F. A review of magnetic solid catalyst development for sustainable biodiesel production. *Biomass Bioenergy* **2021**, *149*, 106099.
(21) Carrera, S. A.; Villarreal, J. S.; Acosta, P. I.; Noboa, J. F.; Gallo-Cordova, A.; Mora, J. R. Designing an efficient and recoverable magnetic nanocatalyst based on Ca, Fe and pectin for biodiesel production. *Fuel* **2022**, *310*, 122456.
(22) Xie, T.; Hu, J.; Yang, J.; Liu, C.; Xu, L.; Wang, J.; Peng, Y.; Liu, S.; Yin, X.; Lu, Y. Visible-Light-Driven Photocatalytic Activity of Magnetic BiOBr/$SrFe_{12}O_{19}$ Nanosheets. *Nanomaterials* **2019**, *9*, 735.
(23) Wang, H.; Xu, L.; Wu, X.; Zhang, M. Eco-friendly Synthesis of a Novel Magnetic $Bi_4O_5Br_2$/$SrFe_{12}O_{19}$Nanocomposite with Excellent Photocatalytic Activity and Recyclable Performance. *Ceram. Int.* **2021**, *47*, 8300−8307.
(24) Wu, G.; Liang, X.; Zhang, L.; Tang, Z.; Al-Mamun, M.; Zhao, H.; Su, X. Fabrication of Highly Stable Metal Oxide Hollow Nanospheres and Their Catalytic Activity toward 4-Nitrophenol Reduction. *ACS Appl. Mater. Interfaces* **2017**, *9*, 18207−18214.
(25) Di Paola, A.; Augugliaro, V.; Palmisano, L.; Pantaleo, G.; Savinov, E. Heterogeneous Photocatalytic Degradation of Nitrophenols. *J. Photochem. Photobiol., A* **2003**, *155*, 207−214.
(26) Cao, H.-L.; Huang, H.-B.; Chen, Z.; Karadeniz, B.; Lü, J.; Cao, R. Ultrafine Silver Nanoparticles Supported on a Conjugated Microporous Polymer as High-Performance Nanocatalysts for Nitrophenol Reduction. *ACS Appl. Mater. Interfaces* **2017**, *9*, 5231−5236.
(27) Dong, Z.; Le, X.; Dong, C.; Zhang, W.; Li, X.; Ma, J. Ni@Pd Core-Shell Nanoparticles Modified Fibrous Silica Nanospheres as Highly Efficient and Recoverable Catalyst for Reduction of 4-Nitrophenol and Hydrodechlorination of 4-Chlorophenol. *Appl. Catal., B* **2015**, *162*, 372−380.
(28) Wu, X.-Q.; Zhao, J.; Wu, Y.-P.; Dong, W.-w.; Li, D.-S.; Li, J.-R.; Zhang, Q. Ultrafine Pt Nanoparticles and Amorphous Nickel Supported on 3D Mesoporous Carbon Derived from Cu-Metal−Organic Framework for Efficient Methanol Oxidation and Nitrophenol Reduction. *ACS Appl. Mater. Interfaces* **2018**, *10*, 12740−12749.
(29) Lee, H.-R.; Park, J. H.; Raza, F.; Yim, D.; Jeon, S.-J.; Kim, H.-I.; Bong, K. W.; Kim, J.-H. Photoactive WS2Nanosheets Bearing Plasmonic Nanoparticles for Visible Light-Driven Reduction of Nitrophenol. *Chem. Commun.* **2016**, *52*, 6150−6153.
(30) Schrinner, M.; Ballauff, M.; Talmon, Y.; Kauffmann, Y.; Thun, J.; Möller, M.; Breu, J. Single Nanocrystals of Platinum Prepared by Partial Dissolution of Au-Pt Nanoalloys. *Science* **2009**, *323*, 617.
(31) Qin, Y.; Zhang, H.; Tong, Z.; Song, Z.; Chen, N. A Facile Synthesis of Fe3O4@SiO2@ZnO with Superior Photocatalytic Performance of 4-nitrophenol. *J. Environ. Chem. Eng.* **2017**, *5*, 2207−2213.
(32) Xiong, R.; Lu, C.; Wang, Y.; Zhou, Z.; Zhang, X. NanofibrillatedCellulose as the Support and Reductant for the Facile Synthesis Of Fe_3O_4/Ag Nanocomposites with Catalytic and Antibacterial Activity. *J. Mater. Chem. A* **2013**, *1*, 14910−14918.
(33) Liu, W.; Sun, D.; Fu, J.; Yuan, R.; Li, Z. Assembly of Evenly Distributed Au Nanoparticles on Thiolated Reduced Graphene Oxide as an Active and Robust Catalyst for Hydrogenation of 4-Nitroarenes. *RSC Adv.* **2014**, *4*, 11003−11011.
(34) Anantharamaiah, P. N.; Mondal, S.; Manasa, K. S.; Saha, S.; Pai M, M. Enhancing the catalytic activity of recyclable nanocrystalline $NiFe_2O_4$ by replacing Ni by Cu. *Ceram. Int.* **2020**, *46*, 1220−1226.
(35) Gurnule, W. B.; Katkamwar, S. S. Analytical Applications of Newly Synthesized Copolymer Resin Derived from P-aminophenol, Dithiooxamide, and Formaldehyde. *J. Appl. Polym. Sci.* **2012**, *123*, 1421−1427.
(36) Shimoga, G.; Palem, R. R.; Lee, S.-H.; Kim, S.-Y. Catalytic Degradability of p-Nitrophenol Using Ecofriendly Silver Nanoparticles. *Metals* **2020**, *10*, 1661.
(37) Cui, Y.; Ma, K.; Chen, Z.; Yang, J.; Geng, Z.; Zeng, J. Atomic-level insights into strain effect on p-nitrophenol reduction via Au@Pd core−shell nanocubes as an ideal platform. *J. Catal.* **2020**, *381*, 427−433.
(38) Pandey, S.; Mishra, S. B. Catalytic reduction of p-nitrophenol by using platinum nanoparticles stabilised by guar gum. *Carbohydr. Polym.* **2014**, *113*, 525−531.
(39) Kästner, C.; Thünemann, A. F. Catalytic Reduction of 4-Nitrophenol Using Silver Nanoparticles with Adjustable Activity. *Langmuir* **2016**, *32*, 7383−7391.
(40) Goyal, A.; Bansal, S.; Singhal, S. Facile Reduction of Nitrophenols: Comparative Catalytic Efficiency of MFe_2O_4 (M = Ni, Cu, Zn) Nanoferrites. *Int. J. Hydrogen Energy* **2014**, *39*, 4895−4908.
(41) Singh, C.; Goyal, A.; Singhal, S. Nickel-doped cobalt ferrite nanoparticles: efficient catalysts for the reduction of nitroaromatic compounds and photo-oxidative degradation of toxic dyes. *Nanoscale* **2014**, *6*, 7959−7970.
(42) Wang, L.; Bao, J.; Wang, L.; Zhang, F.; Li, Y. One-Pot Synthesis and Bio-application of Amine-Functionalized Magnetite Nanoparticles and Hollow Nanospheres. *Chem. - Eur. J.* **2006**, *12*, 6341−6347.
(43) Du, C.; Bai, Y.; Shui, Y.; Zhao, Y.; Zheng, X.; Guo, S.; Wang, Q.; Yang, T.; Wang, S.; Dong, W.; Wang, L. Carbon-Based Nanorod Catalysts for Nitorphenol Reduction. *ACS Appl. Nano Mater.* **2019**, *2*, 879−889.
(44) An, M.; Cui, J.; Wang, L. Magnetic Recyclable Nanocomposite Catalysts with Good Dispersibility and High Catalytic Activity. *J. Phys. Chem. C* **2014**, *118*, 3062−3068.
(45) Ramana, C. V.; Battu, A. K.; Dubey, P.; Lopez, G. A. Phase-Control-Enabled Enhancement in Hydrophilicity and Mechanical Toughness in Nanocrystalline Tungsten Oxide Films for Energy-Related Applications. *ACS Appl. Nano Mater.* **2020**, *3*, 3264−3274.
(46) Ansari, S. M.; Sinha, B. B.; Phase, D.; Sen, D.; Sastry, P. U.; Kolekar, Y. D.; Ramana, C. V. Particle Size, Morphology, and Chemical Composition Controlled $CoFe_2O_4$ Nanoparticles with Tunable Magnetic Properties via Oleic Acid Based Solvothermal Synthesis for Application in Electronic Devices. *ACS Appl. Nano Mater.* **2019**, *2*, 1828−1843.
(47) Anantharamaiah, P. N.; Chandra, N. S.; Shashanka, H. M.; Kumar, R.; Sahoo, B. Magnetic and catalytic properties of Cu-substituted $SrFe_{12}O_{19}$ synthesized by tartrate-gel method. *Adv. Powder Technol.* **2020**, *31*, 2385−2393.
(48) Anantharamaiah, P. N.; Mondal, S.; Saha, S. Inducing the Catalytic Activity in $SrFe_{12}O_{19}$Via Chemical Modification. *Catal. Lett.* **2021**, *151*, 221−231.
(49) Anantharamaiah, P. N.; Joy, P. A. Magnetic and magnetostrictive properties of aluminium substituted cobalt ferrite synthesized by citrate-gel method. *J. Mater. Sci.* **2015**, *50*, 6510−6517.
(50) Anantharamaiah, P. N.; Joy, P. A. Enhancing the strain sensitivity of $CoFe_2O_4$ at low magnetic fields without affecting the magnetostriction coefficient by substitution of small amounts of Mg for Fe. *Phys. Chem. Chem. Phys.* **2016**, *18*, 10516−10527.
(51) Shannon, R. D. Revised effective ionic radii and systematic studies of interatomic distances in halides and chalcogenides. *Acta Crystallogr., Sect. A* **1976**, *32*, 751−767.
(52) Puli, V. S.; Adireddy, S.; Ramana, C. V. Chemical bonding and magnetic properties of gadolinium (Gd) substituted cobalt ferrite. *J. Alloys Compd.* **2015**, *644*, 470−475.

https://doi.org/10.1021/acsomega.1c05548
ACS Omega 2022, 7, 6549−6559

(53) Ramana, C. V.; Hussain, O. M.; Pinto, R.; Julien, C. M. Microstructural features of pulsed-laser deposited V_2O_5 thin films. *Appl. Surf. Sci.* **2003**, *207*, 135−138.
(54) Dânoun, K.; Tabit, R.; Laghzizil, A.; Zahouily, M. A novel approach for the synthesis of nanostructured Ag_3PO_4 from phosphate rock: high catalytic and antibacterial activities. *BMC Chem.* **2021**, *15*−*42*, 1−12.
(55) Abay, A. K.; Chen, X.; Kuo, D.-H. Highly efficient noble metal free copper nickel oxysulfide nanoparticles for catalytic reduction of 4-nitrophenol, methyl blue, and rhodamine-B organic pollutants. *New J. Chem.* **2017**, *41*, 5628−5638.

https://doi.org/10.1021/acsomega.1c05548
ACS Omega 2022, 7, 6549−6559